The Role of Detection Times in Reflectivity Estimation with Single-Photon Lidar

Ruangrawee Kitichotkul, *Student Member, IEEE,* Joshua Rapp, *Member, IEEE,* and Vivek K Goyal, *Fellow, IEEE*

(Invited Paper)

***Abstract*—In direct time-of-flight single-photon lidar, the photon detection times are typically used to estimate the depth, while the number of detections is used to estimate the reflectivity. This paper examines the use of detection times in reflectivity estimation with a free-running SPAD by proposing new estimators and unifying previous results with new analysis. In the low-flux regime where dead times are negligible, we examine the Cramér-Rao bound of reflectivity estimation. When depth is unknown, we show that an estimator based on censoring can perform almost as well as a maximum likelihood estimator, and, surprisingly, incorrect depth estimation can reduce the mean-squared errors of reflectivity estimation. We also examined joint estimation of signal and background fluxes, for which our proposed censoring-based estimator performs as well as the maximum likelihood estimator. In the high-flux regime where dead times are not negligible, we model the detection times as a Markov chain and examine some reflectivity estimators that exploit the detection times.**

***Index Terms*—dead time, direct time of flight, Fisher information, Poisson processes, single-photon avalanche diode, time-correlated single-photon counting.**

I. Introduction

Lidar (sometimes described as an acronym for *light detection and ranging* but originally a portmanteau of *light* and *radar* [1]) uses echoes detected from optical-wavelength illuminations to reveal properties of the surrounding environment. By neglecting subsurface scattering, partial transmission, multiple reflections, and deviation from monostatic geometry, one can simply view lidar as making a measurement along a straight line from a laser illumination source in the imaging apparatus, to a scene patch, and back to the imager. Though estimating the distance of light travel is often the primary or sole objective, reflectivity information is also present. Lidar is thus a method for 3D imaging that can yield both a depth map and an intensity image. Reflectivity images from lidar have been used to aid robots' simultaneous localization and mapping (SLAM) [2] and odometry [3], [4]. Reflectivity in multispectral and hyperspectral lidar can also reveal material properties, and it has been used to classify ores [5], rocks [6], and tree species [7].

In single-photon lidar (SPL), the illumination consists of a sequence of very short pulses and the detector has single-photon sensitivity. Reflectivity information has been important to recent progress in SPL toward accurate depth mapping from very few detected photons [8], [9], [10], [11], [12] and with low signal-to-background ratio (SBR) [13], [14], [15]. Key themes of these works include using intensity as a cue for local SBR and exploiting the tendency for depth and intensity edges to appear at the same locations. Thus, these works are benefiting from the joint estimation of reflectivity and depth through the incorporation of assumptions about scene structure. They may misleadingly suggest that when considering a single pixel in isolation, the depth and reflectivity information are decoupled, with detection times revealing depth and numbers of detections revealing reflectivity.

In this paper, we examine the joint estimation of reflectivity and depth at a single pixel (i.e., without spatial regularization), with an emphasis on the accuracy of reflectivity. We determine and illustrate certain fundamental limits of performance for a variety of settings. In particular, we illustrate that photon detection times are informative in reflectivity estimation, perhaps contrary to intuition that only numbers of detections are informative. Some previous works have exploited detection times to censor the detection events imputed to ambient light, but they then emphasize the impact on depth estimation [9], [13]. One of our findings is that censoring can improve reflectivity estimation as well. Similar to time gating, censoring removes background detections, which contribute most to the error when SBR is low. Moreover, with either censoring or maximum likelihood estimation, incorrect depth estimation can surprisingly reduce the mean-squared errors of reflectivity estimation. We also examined joint estimation of signal and background fluxes, for which our proposed censoring-based estimator performs as well as the maximum likelihood estimator.

The literature on SPL with time-correlated single-photon counting (TCSPC) is complicated by variations on the protocol for data collection; the level of detail of the data that is retained; free-running vs. synchronous modes; and whether dead time effects are negligible. We present here a taxonomy of these variations and develop results for the most interesting cases. Some elements of this paper are tutorial, serving to unify and clarify results from [9], [13], [16], [17], [18]. New results include maximum likelihood (ML) estimators of the reflectivity and the depth with respect to the detection times for both the low- and high-flux regimes. In the low-flux case, we provide a Fisher information analysis and evaluate the proposed ML reflectivity estimator along with other estimators for comparison via simulation. The mean-squared errors of the ML estimator and a censoring-based estimator are almost identical across the range of SBRs from 0.01 to 1.0 with

R. Kitichotkul and V. K. Goyal are with the Department of Electrical and Computer Engineering, Boston University, Boston, MA 02215 USA (rkitich@bu.edu; v.goyal@ieee.org).

J. Rapp is with Mitsubishi Electric Research Laboratories, Cambridge, MA 02139 USA (rapp@merl.com).

R. Kitichotkul and V. K. Goyal were supported by the US National Science Foundation under Grants 1955219 and 2039762. This work was completed in part while J. Rapp was with Boston University.

average numbers of detected signal photons ranging from 2 to 10. This result suggests that censoring is an effective and efficient way to estimate the reflectivity in the low-flux case.

A. Related Work

The most well-known early developments of SPL using avalanche photodiodes diodes were due to teams at MIT Lincoln Laboratory [19], [20], [21], [22], [23] and Heriot-Watt University [24], [25], [26], [27], [28], [29]. These groups developed single-photon avalanche diode (SPAD) technology, time measurement circuitry, and prototype systems.

By demonstrating reasonable 3D imaging accuracy with 1 detected photon per pixel and SBR of 1, first-photon imaging [8] inspired many SPL works in which advances in probabilistic modeling and computational methods are of paramount importance. These include works addressing the challenges associated with having very few detected photons [9], [30], [31], [10], [11], strong background light [13], [14], [32], [33], very long range [34], [35], [36], obscurants [37], [38], [39], scenes with multiple layers [40], [12], [41], [42], and real-time reconstruction [43], [44], [45]. Other works addressed data processing to mitigate hardware limitations, such as dead times [46], [47], [48], [16], [49], [50], [51], [17], [52], analog-to-digital-converter trade-offs [53], [54], and data throughput [55], [56], [57].

Ballistic missile identification and detection of obscured targets motivated some initial SPL development [23], and early commercial technology was a direct offshoot of the U.S. Defense Advanced Research Project Agency's *Grand Challenge* [58]. Now, SPADs are becoming cheaper and easier to manufacture using standard CMOS processes. As a result, SPL is a common component for autonomous vehicles [59], and it is embedded in high-end consumer electronics devices such as the iPad Pro and iPhone 12–14 Pro [60], and even for low-cost range or proximity sensing [61], [62]. Applications include atmospheric measurement [63], geoscience [64], [65], [66], and cultural heritage preservation [67].

B. Outline

The remainder of the paper is organized as follows. Section II characterizes the photon arrival process and describes how nonidealities in a SPAD, such as dead times, affect the detection model. Section III explores how different possibilities in the flux levels, data collection protocols, and prior knowledge about the scene affect the detection model and the resulting estimation problem. Section IV examines the reflectivity estimation problem in the low-flux regime, where dead time effects are negligible. We describe the probability distribution of the detection times and study some estimators in the low-flux regime. Then, we provide a Fisher information analysis of the reflectivity and an evaluation of the estimators based on simulation results. Section V examines the reflectivity estimation problem in the high-flux regime, where dead time effects cannot be ignored. We model a sequence of detections as a Markov chain and discuss some estimators.

II. Single-Photon Detection with SPADs

A typical model for SPL assumes that the illuminated target is a single opaque, Lambertian surface at a fixed distance z from the laser. We develop here a mathematical model for the detection times when the surface is illuminated n_{r} times by a periodically-pulsed laser source with repetition period t_{r}. The sequence of arriving photons is a realization of an inhomogeneous (time-varying) Poisson process with periodic rate function [68], [69]. If the laser pulses are emitted at times $t = nt_{\mathrm{r}}$ where index $n = 0, 1, \ldots, n_{\mathrm{r}} - 1$, the intensity of the arriving photons is

$$\lambda(t) = \sum_{n=0}^{n_{\mathrm{r}}-1} \widetilde{\lambda}(t - nt_{\mathrm{r}}), \tag{1}$$

where the single-period intensity $\widetilde{\lambda}(t)$ is supported on $[0, t_{\mathrm{r}})$. We now characterize the arrival processes of photons from the laser and other sources in each repetition period.

A. Signal Photons

A single laser pulse has a temporal profile $\rho_{\mathrm{s}} s(t)$, where $s(t)$ satisfies $\int_{-\infty}^{\infty} s(t)\,\mathrm{d}t = 1$, and $\rho_{\mathrm{s}} > 0$ is the laser flux. Photons that were initially emitted by the laser and then reflect off the target back to the detector are called *signal* photons. The illuminated point has reflectivity $\alpha \in [0, 1)$, which includes the effects of surface albedo, view angle, and range-based falloff. The single-period signal intensity is

$$\widetilde{\lambda}_{\mathrm{s}}(t) = \alpha\rho_{\mathrm{s}} s(t - 2z/c), \quad t \in [0, t_{\mathrm{r}}), \tag{2}$$

where c is the speed of light, and $2z/c$ is the time-shift due to the round-trip distance that the laser pulse travels to the target and back. We assume that $2z/c < t_{\mathrm{r}}$, which prevents distance aliasing, i.e., a detected signal photon must have been emitted at the beginning of the current repetition period and not any of the previous periods. We assume that the full width at half maximum (FWHM) pulse width t_{p} is very short in comparison to the repetition period t_{r}, so $\int_0^{t_{\mathrm{r}}} s(t - 2z/c)\,\mathrm{d}t \approx 1$. A useful quantity is the signal flux

$$\Lambda_{\mathrm{s}} = \int_0^{t_{\mathrm{r}}} \widetilde{\lambda}_{\mathrm{s}}(t)\,\mathrm{d}t = \alpha\rho_{\mathrm{s}}, \tag{3}$$

which is the mean number of signal photons arriving during any period. Since the signal photon sequence is a realization of a Poisson process, the number of photon arrivals during a period t_{r} is a Poisson random variable with parameter Λ_{s}. Estimating the reflectivity of a scene is equivalent to estimating the signal flux, up to a linear scaling factor. We can rewrite the single-period signal intensity to explicitly include Λ_{s}:

$$\widetilde{\lambda}_{\mathrm{s}}(t) = \Lambda_{\mathrm{s}} s(t - 2z/c), \quad t \in [0, t_{\mathrm{r}}). \tag{4}$$

B. Background Photons

The other main source of photons arriving at the detector is ambient light that, in isolation, contains no information about the target distance. We call these *background* photons and assume the total acquisition time $n_{\mathrm{r}} t_{\mathrm{r}}$ is short enough that the ambient light power is constant over the acquisition

time. Although background photons may be emitted from sources with non-Poissonian statistics, e.g., thermal sources, wavelength filtering ensures the background light reaching the detector is quasi-monochromatic, and Poisson statistics are a good approximation [68]. The sequence of photons is modeled as a homogeneous Poisson process with constant intensity. We denote the single-period intensity by $\widetilde{\lambda}_{\mathrm{b}}(t) = b$ for $t \in [0, t_{\mathrm{r}})$. Because the background intensity is constant, the background flux (the expected number of background photons arriving during a period of duration t_{r}) is trivially $\Lambda_{\mathrm{b}} = bt_{\mathrm{r}}$. We note that when the ambient light fluctuates slowly enough, assuming that the background intensity is constant in each repetition period can be a good approximation. Many results in Sections IV and V may be extended to scenarios with fluctuating background in this case.

C. Total Arrival Process

The signal and background processes are statistically independent, so the sequence of all photons arriving at the detector is described by the superposition of the signal and background processes and is likewise a Poisson process. The single-period total arrival process intensity is

$$\widetilde{\lambda}(t) = \widetilde{\lambda}_{\mathrm{s}}(t) + \widetilde{\lambda}_{\mathrm{b}}(t) \tag{5}$$

$$= \Lambda_{\mathrm{s}} s(t - 2z/c) + b, \quad t \in [0, t_{\mathrm{r}}), \tag{6}$$

which sums the intensities of the signal and background processes. Similarly, the total flux $\Lambda = \Lambda_{\mathrm{s}} + \Lambda_{\mathrm{b}} = \alpha\rho_{\mathrm{s}} + bt_{\mathrm{r}}$ sums the component fluxes. The total arrival process over the acquisition time $n_{\mathrm{r}}t_{\mathrm{r}}$ is therefore

$$\lambda(t) = \Lambda_{\mathrm{s}} \left[\sum_{n=0}^{n_{\mathrm{r}}-1} s(t - 2z/c - nt_{\mathrm{r}}) \right] + b. \tag{7}$$

We note that more complicated scenes will affect the photon arrival model. For instance, rapidly changing lighting conditions would lead to an inhomogenous background process. Alternatively, partial reflections at object edges or through semi-transparent media would cause the signal process to include multiple distinct reflections [40], [41], [42], [12], [43]. Surfaces at oblique angles, especially at long range, will reflect a broadened pulse shape relative to the illumination pulse [70]. Furthermore, scattering media such as fog would introduce an additional classification of *scattered* photons that were emitted by the laser and interact with the medium rather than the target before detection [38]. Although we will focus only on the simple case, reflectivity and depth estimation for the more complex scenarios can be extrapolated from the simple estimators with some modification.

D. Detection Efficiency and Dark Counts

Despite improvements in single-photon detectors and timing electronics, not every photon arriving at a detector can be registered as a count. We consider the detection model for SPADs, which have become ubiquitous in SPL applications because of the many benefits of solid-state devices, including room-temperature operation, ruggedness, and low bias voltage compared to photomultiplier tubes (PMTs) and superconducting nanowire single-photon detectors (SNSPDs).

A SPAD is a reverse-biased photodiode biased above the breakdown voltage [71]. When a photon reaches the active area of the SPAD, it causes the generation of a photoelectron with a probability described by the quantum efficiency. If a photoelectron is generated, the potential across the diode accelerates the electron, causing an avalanche of charge carriers (electrons and holes). The sharp increase in current from the avalanche causes a detection event to be recorded by the TCSPC timing electronics.

The probability that an arriving photon both generates a photoelectron and produces a detectable avalanche current is called the *detection efficiency* η [72]. The detection efficiency effectively multiplies each photon arrival by a Bernoulli random variable with parameter η to determine whether an arriving photon is detected. Since the Bernoulli random variable is independent of the arrival process, the detection process is a "thinned" version of the arrival process and is still a Poisson process [69]. The single-period intensity of the detection process is $\eta\widetilde{\lambda}(t)$.

Photoelectrons are not the only triggers for a carrier avalanche. Dark counts are spurious detection events caused by thermal noise rather than incident photons [71]. By modeling dark counts as a homogeneous Poisson process [9], we add the dark count rate b_{d} to the detection process intensity.

The detection process intensity, including detection efficiency and dark counts, for a single period is thus

$$\eta\widetilde{\lambda}(t) + b_{\mathrm{d}} = \eta\Lambda_{\mathrm{s}} s(t - 2z/c) + \eta b + b_{\mathrm{d}}. \tag{8}$$

This detection process intensity can be written in the form of the single-period arrival process intensity in (6) with simple redefinitions of the notation: $\Lambda_{\mathrm{s}} := \eta\Lambda_{\mathrm{s}}$ and $b := \eta b + b_{\mathrm{d}}$. Since this scaling and shifting is trivial, we assume $\eta = 1$ and $b_{\mathrm{d}} = 0$ for simplicity; in the detection process intensity (7), the detection efficiency and dark counts are modeled implicitly.

E. Afterpulsing and Dead Times

During the charge carrier avalanche in a SPAD, additional photon arrivals cannot be recorded, since a single photoelectron will make no meaningful difference to the avalanche. Thus, each avalanche must be quenched via passive or active circuitry to stop the flow of charge and reset the SPAD to an armed state. Despite the quenching process, charge carriers may become trapped in defects in the SPAD, and the time until detrapping of the carriers is modeled as an exponential random variable [71]. If the SPAD is armed when detrapping occurs, another carrier avalanche may ensue and be registered as an event detection. This process is called *afterpulsing* because it leads to spurious detections that are statistically dependent on the most recent avalanche time.

To minimize the effect of afterpulsing, SPADs are not immediately reset after quenching. Instead, they are kept unarmed for an additional hold-off period, during which carriers can detrap without being detected [71]. We refer to the entire period of quenching and hold-off as the *detector dead time* since incident photons also cannot be detected. There is thus an

inherent trade-off in the duration of the dead time, since longer dead times reduce the probability of afterpulsing but also prevent further photon detections. This trade-off is exacerbated for infrared-sensitive SPADs, such as InGaAs/InP devices, which have higher dark count rates than the Si SPADs that are sensitive to visible wavelengths. Cooling the detectors decreases the dark count rate, at the expense of increasing the detrapping lifetime, so longer hold-off times are advantageous to reduce the number of detected afterpulses [73].

The dead time duration is further complicated by two competing approaches for deciding when to reset the detector. The *synchronous* (also known as "clock-driven") approach synchronizes the reset to the illumination repetition period to ensure the detector is always armed at the start of a repetition period [74]. Only the first photon arriving during each period is detected, and the resulting dead time duration is randomized by the relative detection time within the illumination period. Synchronous reset results in statistically independent illumination periods, which can facilitate simplified detection modeling. However, the preference towards detecting early arrivals results in a distance-dependent skew in the distribution of detection times, which is especially problematic when the background flux is large [75], [47], [48], [50].

On the other hand, the *asynchronous* (also known as "event-driven," "photon-driven," or "free-running") approach uses a fixed dead time of duration t_d following each photon detection [74]. Asynchronous reset is independent of the illumination time, thus enabling multiple photons to be detected in a single illumination period if $t_\mathrm{d} < t_\mathrm{r}$ or allowing for the dead time starting in one period to carry over into the start of the next period. A consequence of this behavior is that the detection process is not statistically independent between illumination periods, thus requiring more sophisticated modeling [16], [52].

A further consideration is the use of time-gated detection, which allows detection to occur during a pre-specified "gate" window, defined relative to the illumination period, and suppresses detection outside of the gate. Gating can be useful for ignoring background detections when the scene of interest is known to exist within a range of distances smaller than the unambiguous range set by the repetition period. Gating can further turn an asynchronous system into a synchronous one, if the gate-off time is longer than t_d, ensuring that the detector is always armed at the gate-on time.

Finally, we must consider the TCSPC electronics that tag each SPAD detection event with a high-resolution time stamp. Not only the SPADs but also the TCSPC electronics can exist in synchronous or asynchronous variants. For instance, TCSPC electronics combining time-to-amplitude converters (TACs) with analog-to-digital converters (ADCs) are typically synchronous, whereas electronics based on time-to-digital converters (TDCs) are often asynchronous, with a fixed dead time t_e during which the detection time is processed and stored.

In this work, we assume both the SPAD and TCSPC electronics are asynchronous, which affects the model as explored in Section V. We further assume that the detector dead time t_d is long enough to make afterpulsing sufficiently unlikely and indistinguishable from dark counts.

F. Detection Times and Counts

Denote the number of detections during period $[0, n_\mathrm{r} t_\mathrm{r})$ by N, and denote the sequence of *absolute detection times* by $\{T_i\}_{i=1}^N$. For each i, define a *relative detection time* through reduction modulo t_r:

$$T_i = M_i t_r + \widetilde{T}_i, \qquad \widetilde{T}_i \in [0, t_\mathrm{r}), \quad M_i \in \mathbb{Z}. \tag{9}$$

Then the set of pairs $\{(\widetilde{T}_i, M_i)\}_{i=1}^N$ is equivalent to the sequence of absolute detection times, with $\{\widetilde{T}_i\}_{i=1}^N$ being the sequence of detection times relative to the most recent pulse emissions and $\{M_i\}_{i=1}^N$ indicating the period indexes of the detections.

By definition, absolute detection times are an increasing sequence. The period indexes are nondecreasing, and the relative detection times satisfy no ordering property. To avoid possible confusion with our notation, the period indexes $\{M_i\}_{i=1}^N$ and relative detection times $\{\widetilde{T}_i\}_{i=1}^N$ are to be interpreted as multisets in the case of repeated values.

III. Taxonomy of Estimation Problems

A. Flux Conditions

Perhaps the key property determining the acquisition model is the photon flux. When the detectable flux is low (e.g., $\Lambda \ll 1$), the probability of a photon arriving during a dead time is negligible, so it is reasonable to assume that there are no missed detections. Thus the particular details of the acquisition system can be ignored, and the detection sequence can be considered equivalent to the photon arrival sequence, i.e., a realization of a Poisson process. As the flux increases, the probability of photons arriving during a dead time increases. Taking the missed detections into account requires carefully modelling the time-dependence of the dead times, such as specifying whether the system has synchronous or asynchronous dead times.

B. Data Collection and Retention Protocols

1) Data Collection Duration: The vast majority of the SPL literature assumes n_r is deterministic and known, as this describes hardware systems that raster scan a sequence of laser positions with a pre-specified duration for each position. A few works have proposed adaptive approaches that could improve the efficiency of scanning, depending on the scene content. First-photon imaging proposed using exactly one detected photon per scene pixel—i.e., fixing $N = 1$—so that reflectivity information is contained only in the geometrically distributed number of illuminations n_r before the first photon is detected [8]. Medin et al. considered the data collection duration as a resource allocation problem, in which both the number of illuminations n_r and the number of counts N were allowed to vary in order to minimize the error in the reflectivity estimate [76]. We will only consider n_r to be deterministic and known in the remainder of the paper.

2) Data Retention: The full data set generated from n_r repetition periods is a number of detections N and the absolute detections times $\{T_i\}_{i=1}^N$ or, equivalently, $\{(\widetilde{T}_i, M_i)\}_{i=1}^N$. Some reductions of this data set are quite common, and whether the reduction degrades the ability to estimate the target parameters depends on the imaging scenario.

An unordered multiset of values (also referred to as a histogram, empirical distribution, or type) derived from a sequence fundamentally contains less information than the sequence [77], but it may contain all the information relevant to an estimation problem. If the sequence is generated from independent trials of an experiment and the goal is to estimate parameters of the experiment, then the order of outcomes is irrelevant; when the trials are not independent, the order may be relevant.

The vast majority of SPL techniques are based on retaining only the histogram of relative detection times, which implicitly contains N. It is possible to have slightly less information by retaining only a normalized histogram, thus essentially losing the value of N. Many possibilities exist between only the histogram of relative detection times and the full sequence of absolute detection times. For example, one could retain separate histograms of both the relative detection times and the period index increments $M_i - M_{i-1}$.

As we discuss in Section IV, low flux implies approximate independence of disjoint sets of repetition periods; thus, $\{\widetilde{T}_i\}_{i=1}^N$ is as informative as $\{(\widetilde{T}_i, M_i)\}_{i=1}^N$ for our estimation problems, so we may retain only the former which demands less memory. In the high-flux regime, however, the absolute detection times $\{T_i\}_{i=1}^N$ contain information about the scene parameters not present in the relative detection time histogram; details are discussed in Sections IV and V.

C. Prior Knowledge

The prior knowledge about the scene determines which models and estimators are applicable. For example, the detection model introduced in Section II assumes that multiple reflections are negligible, so the returning signal is the outgoing laser pulse shifted by $2z/c$ in time. Otherwise, hardwiring z into the detection model may be inappropriate. Alternatively, some works allow the impulse response to be arbitrary and then, following the Bayesian paradigm, impose priors according to knowledge about the scene. For example, sparsity in time achieved through ℓ_1 regularization [40] and a union-of-subspace approach [31] have been used when there are few partially reflecting surfaces in the illumination path. Moreover, this modeling naturally facilitates spatiotemporal priors [78], [42]. Priors for reflectivity and background flux that exploit spatial correlation between pixels have also been proposed [12].

Even when we assume the detection model in Section II, the knowledge of Λ_s, Λ_b, or z determines the applicable estimators and, consequently, the accuracy and computation requirement. While maximizing the likelihood functions (12) in the low-flux case or (36) in the high-flux case with respect to Λ_s, Λ_b, and z can jointly estimate all three parameters, the computation may not be tractable. Alternatively, when z is known, convex optimization algorithms can efficiently maximize both likelihoods to estimate Λ_s and Λ_b.

IV. Low-flux Reflectivity Estimation

When the total flux is low, i.e., $\Lambda \ll 1$, the probability of a photon arriving during the dead time following a previous detection is negligible. Historically, a threshold of $\Lambda < 5\%$ has been commonly used [79]. When the dead times are negligible, detections are modeled as arrivals in an inhomogeneous Poisson process characterized by intensity function (7). Thus, N is a Poisson random variable with parameter $n_\mathrm{r}\Lambda$, so its probability mass function (PMF) is

$$p_N(n) = \frac{(n_\mathrm{r}\Lambda)^n \exp\left(-n_\mathrm{r}\Lambda\right)}{n!}. \tag{10}$$

Conditioned on $N = n$, the relative detection times $\{\widetilde{T}_i\}_{i=1}^n$ are independent and identically distributed with conditional probability distribution function (PDF)

$$f_{\widetilde{T}_i|N}(\tilde{t}_i \,|\, n) = \frac{\widetilde{\lambda}(\tilde{t}_i)}{\Lambda}. \tag{11}$$

One of the major simplifications that follows from neglecting dead times is that each repetition period becomes an independent and identically distributed trial. Hence, the relative detection times are as informative as the absolute detection times in the low-flux setting. The joint density of the number of detections N and the detection times $\widetilde{T}_1, \ldots, \widetilde{T}_N$ during $[0, n_\mathrm{r}t_\mathrm{r})$, is

$$\begin{aligned} &f_{N,\widetilde{T}_1,\ldots,\widetilde{T}_N}(n, \tilde{t}_1, \ldots, \tilde{t}_n) \\ &\qquad = \left(\prod_{i=1}^n \frac{\widetilde{\lambda}(\tilde{t}_i)}{\Lambda}\right) \frac{(n_\mathrm{r}\Lambda)^n \exp\left(-n_\mathrm{r}\Lambda\right)}{n!}. \end{aligned} \tag{12}$$

A. Background Flux Estimation

The background flux Λ_b can be estimated in a calibration step in which the laser is turned off. During background calibration, the detection process is a homogeneous Poisson process with intensity $\lambda_\mathrm{b}(t) = b$, so the ML estimate of the background intensity given the number of detections N over a background calibration time t_b is

$$\hat{b} = \frac{N}{t_\mathrm{b}}. \tag{13}$$

The corresponding background flux estimate is $\hat{\Lambda}_\mathrm{b} = \hat{b}t_\mathrm{r} = Nt_\mathrm{r}/t_\mathrm{b}$. In the following, we assume that the background flux Λ_b or its estimate is known.

B. Signal Flux Estimation

1) ML Estimation from Detection Counts: Initial works in photon-efficient SPL used only the count N and the calibrated Λ_b to estimate the signal flux Λ_s [9], [80]. Since the number of signal counts is Poisson, maximizing the likelihood in (10) yields a constrained ML estimate

$$\hat{\Lambda}_\mathrm{s} = \max\left\{\frac{N}{n_\mathrm{r}} - \Lambda_\mathrm{b}, 0\right\}. \tag{14}$$

However, the estimate (14) ignores the information in the detection times.

2) ML Estimation from Detection Times: An ML estimator of Λ_s based on the relative detection times $\{\widetilde{T}_i\}_{i=1}^N$ can be computed by maximizing the likelihood in (12). Unless the depth z is known, we need to maximize the likelihood with respect to z as well. The joint ML estimation of Λ_s and z using relative detection times amounts to solving the following optimization problem:

$$\max_{\hat{\Lambda}_\mathrm{s}\geq 0,\ \hat{z}\in[0,ct_\mathrm{r}/2)} -n_\mathrm{r}\hat{\Lambda}_\mathrm{s} + \sum_{i=1}^{n} \log\left(\hat{\Lambda}_\mathrm{s} s(\tilde{t}_i - 2\hat{z}/c) + b\right). \tag{15}$$

While the maximization objective in (15) is concave in $\hat{\Lambda}_\mathrm{s}$, it is nonconcave in $\hat{z}$ for a typical pulse shape $s(t)$. In general, computing the ML estimate $\hat{\Lambda}_\mathrm{s}$ in (15) is difficult unless the depth z is known. We note that if $\hat{\Lambda}_\mathrm{s}$ is fixed, then maximizing the objective in (15) with respect to $\hat{z}$ is equivalent to finding the time shift that maximizes the output of a log-matched filter [9], [13], [81]. However, to find the global optimal point, a brute force search over $\hat{\Lambda}_\mathrm{s}$ and $\hat{z}$ may be necessary.

3) Approximate ML Estimation via Censoring: Since jointly solving for the ML flux and depth estimators can be computationally inefficient, an ad hoc simplification was proposed in [13]. The main idea is that the ML estimates become uncoupled if $b = 0$, so estimation is dramatically simplified if the background detections can be identified and removed. A proxy for identifying background detections is to use $\{\widetilde{T}_i\}_{i=1}^N$ to choose a cluster of detection times that likely belong to the signal photons, and then estimate Λ_s using that cluster. For example, in Neyman-Pearson censoring [13], the largest cluster in a time window of size t_win is treated as containing most of signal detections if the number of detections N_cl in the time window is sufficiently large according to a hypothesis test. The signal flux estimator in [13] modifies (14) to include only the detection count within the window:

$$\hat{\Lambda}_\mathrm{s} = \max\left\{\frac{N_\mathrm{cl}}{n_\mathrm{r}} - \Lambda_\mathrm{b}\frac{t_\mathrm{win}}{t_\mathrm{r}}, 0\right\}. \tag{16}$$

We note that even if the largest cluster does not actually contain any signal photon, N_cl still contains information about Λ_s because it must be larger than the cluster containing the most signal photons. Consequently, whether the Neyman-Pearson censoring's hypothesis test ascribes the cluster to the signal photons or not, the estimator (16) may be accurate regardless.

C. Fisher Information Analysis

The Cramér–Rao bound (CRB) identifies a lower bound on the mean-squared error (MSE) of any unbiased estimator as the inverse of Fisher information. The Fisher information about the signal flux Λ_s in the detection times $\{\widetilde{T}_i\}_{i=1}^N$ when z and Λ_b are known is

$$\mathcal{I}(\Lambda_\mathrm{s}) = -\mathbb{E}\left[\frac{\partial^2}{\partial\Lambda_\mathrm{s}^2}\log f_{N,\widetilde{T}_1,\ldots,\widetilde{T}_N}(N,\widetilde{T}_1,\ldots,\widetilde{T}_n)\right] \tag{17}$$

$$= n_\mathrm{r}\Lambda\,\mathbb{E}\left[\left(\frac{s(\widetilde{T}_1 - 2z/c)}{\widetilde{\lambda}(\widetilde{T}_1)}\right)^2\right], \tag{18}$$

where the second equality exploits the fact that $\widetilde{T}_1,\ldots,\widetilde{T}_N$ are independent and identically distributed when conditioning on N. The expectation over $\widetilde{T}_1$ in the Fisher information (18) can be computed using a quadrature with PDF (11). The CRB is then

$$\mathbb{E}\left[(\hat{\Lambda}_\mathrm{s} - \Lambda_\mathrm{s})^2\right] \geq \mathcal{I}(\Lambda_\mathrm{s})^{-1}, \tag{19}$$

where $\hat{\Lambda}_\mathrm{s}$ is any unbiased estimate based on $\{\widetilde{T}_i\}_{i=1}^N$.

When $b = 0$, the Fisher information (18) is reduced to

$$\mathcal{I}(\Lambda_\mathrm{s}) = \frac{n_\mathrm{r}}{\Lambda_\mathrm{s}}, \tag{20}$$

which is identical to the Fisher information about Λ_s in only the detection count N under the same setting. This result is unsurprising, since $\hat{\Lambda}_\mathrm{s}$ in (15) reduces to that in (14) when $b = 0$. In the asymptotically high SBR regime, the locations of the detection times $\{\widetilde{T}_i\}_{i=1}^N$ become irrelevant in estimating Λ_s. This observation further justifies the censoring estimator: the locations of $\{\widetilde{T}_i\}_{i=1}^N$ are most relevant in distinguishing signal detections from background, but with perfect censoring only the count N matters.

When we jointly estimate Λ_s and z with Λ_b known, the CRB instead lower bounds the covariance of an unbiased estimate $[\hat{\Lambda}_\mathrm{s}\ \hat{z}]^\top$ by the inverse of the Fisher information matrix:

$$\mathcal{I}(\Lambda_\mathrm{s}, z) = -\mathbb{E}\begin{bmatrix}\frac{\partial^2\log f}{\partial\Lambda_\mathrm{s}^2} & \frac{\partial^2\log f}{\partial\Lambda_\mathrm{s}\partial z}\\ \frac{\partial^2\log f}{\partial\Lambda_\mathrm{s}\partial z} & \frac{\partial^2\log f}{\partial z^2}\end{bmatrix}, \tag{21}$$

where $f := f_{N,\widetilde{T}_1,\ldots,\widetilde{T}_N}(N,\widetilde{T}_1,\ldots,\widetilde{T}_n)$. We note that $-\mathbb{E}\frac{\partial^2\log p}{\partial\Lambda_\mathrm{s}\partial z} \approx 0$ when the pulse shape $s(t)$ is symmetric and the pulse width is much shorter than the repetition period t_r. Consequently, the CRB in (19) approximately holds even when Λ_s and z are estimated jointly.

We further derive the Fisher information when jointly estimating Λ_b, Λ_s, and z in Appendix A.

D. Simulation Results

Figure 1 shows the root mean-squared error (RMSE) of the signal flux estimators (14), (15), and (16) at a fixed Λ_s and varying Λ_b. The mean number of signal photons in each independent experiment $n_\mathrm{r}\Lambda_\mathrm{s}$ is 2, 6, or 10. The signal-to-background ratio (SBR), defined as $\Lambda_\mathrm{s}/\Lambda_\mathrm{b}$, ranges from 0.01 to 1.00. For the censoring estimator (16), we always produce an estimate with the largest cluster regardless of the result from the Neyman-Pearson censoring hypothesis test. For the ML estimator detection times (15), we use alternating maximization of the objective with respect to $\hat{z}$ and $\hat{\Lambda}_\mathrm{s}$ with an initial $\hat{\Lambda}_\mathrm{s}$ from the censoring estimator (16), which often yields $\hat{\Lambda}_\mathrm{s}$ and $\hat{z}$ that are very close to the global maximum of the but with much less computation. The CRB on the RMSE of an unbiased estimator, which is $\mathcal{I}(\Lambda_\mathrm{s})^{-1/2}$ according to (18) and (19), is also plotted.

According to Figure 1, the censoring estimator (16) and the ML estimator with detection times (15) have very close RMSE across the SBR range, and they both have much lower RMSE than the ML estimator with only counts (14). The RMSE gap between the estimators that use detection times and the one that uses only the count is higher at lower SBR, because the

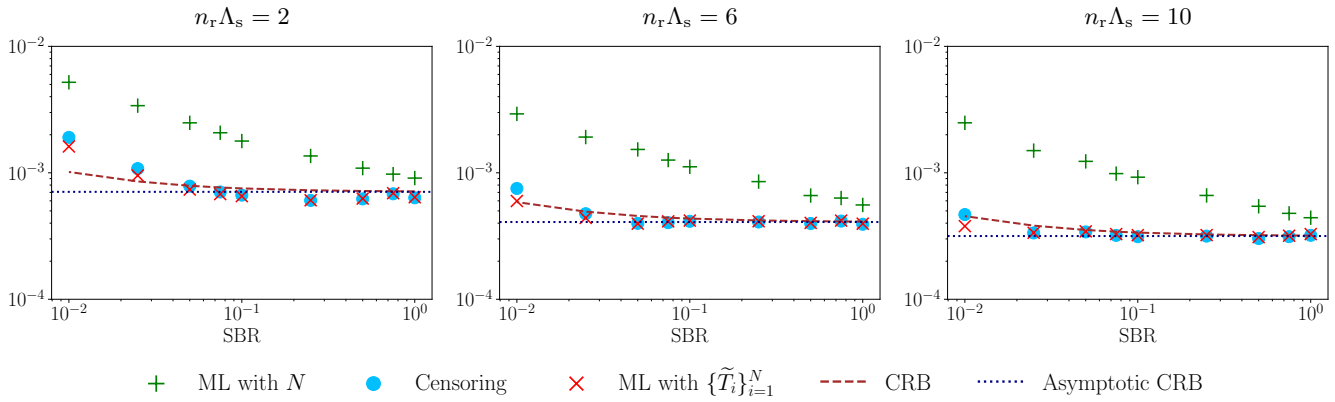

Fig. 1: RMSE of signal flux estimates from simulations under the low flux setting. The true signal flux Λ_s is fixed, and the background flux Λ_b varies. The x-axis is the signal-to-background ratio (SBR). "ML with N" points are estimates based on (14). "Censoring" points are estimates using the censoring approach (16). "ML with $\{\widetilde{T}_i\}_{i=1}^N$" points are estimates based on (15). "CRB" is the Cramér-Rao lower bound on the RMSE of unbiased estimates using detection times (19). "Asymptotic CRB" is the CRB when SBR approaches infinity, which is the square root of the inverse of the Fisher information (20).

background photons account for most of the variance in the count N and thus the corresponding estimate (14). By reducing the contribution from background photons either via censoring in (16) or weighting with the pulse shape $s(t)$ in (15), the estimators based on $\{\widetilde{T}_i\}_{i=1}^N$ achieve lower variance and thus lower RMSE. At higher SBR, the background counts contribute less to the estimate that uses only N (14), so the RMSE gap decreases.

Both the censoring estimator (16) and the ML estimator with detection times (15) have RMSEs close to, and sometimes slightly lower than, the CRB. We note that both estimators jointly estimate Λ_s and z. A closer inspection reveals that their RMSE may become lower than the CRB when $\hat{z}$ significantly differs from the ground truth z. According to Figure 2, the RMSE of the ML estimator (15) decreases below the CRB when $\hat{z}$ is wrong for a certain SBR range. The censoring estimator (16) also displays similar behavior. This phenomenon can be explained in terms of the distribution of the size of a background cluster—for a given mean number of signal photons, there is a range of SBR values with high probability of observing a background cluster of the same size [13]. Moreover, when $\hat{z}$ is wrong, there must be a background cluster that is larger than the cluster containing most of the signal detections. Conditioning on having wrong $\hat{z}$, the estimators have a positive bias but lower variance; thus, they can overcome the CRB.

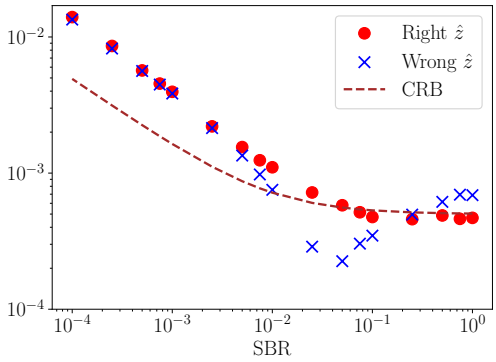

Fig. 2: RMSE of ML signal flux estimates (15) when the depth estimates $\hat{z}$ are right or wrong for $n_r\Lambda_s = 4$. We declare $\hat{z}$ as wrong if it deviates from z by more than three times of the Gaussian pulse's standard deviation. Otherwise, $\hat{z}$ is right.

E. Joint Estimation of Signal Flux and Background Flux

Detection times not only improve reflectivity estimation, but also enable new capabilities. For example, when the background flux Λ_b is unknown and non-zero, the number of detections N alone does not distinguish the signal from the background. We will investigate joint estimation of Λ_s and Λ_b when z is known by exploiting detection times $\{\widetilde{T}_i\}_{i=1}^N$.

1) ML Estimation from Detection Times: The joint ML estimation of Λ_s and Λ_b maximizes the likelihood (12) with respect to the two unknowns.

$$\max_{\hat{\Lambda}_s \geq 0,\ \hat{\Lambda}_b \geq 0} -n_r(\hat{\Lambda}_s + \hat{\Lambda}_b) + \sum_{i=1}^{n} \log\left(\hat{\Lambda}_s s(\tilde{t}_i - 2z/c) + \frac{\hat{\Lambda}_b}{t_r}\right) \tag{22}$$

Different from the optimization problem (15), where the objective is nonconcave in the unknown variable $\hat{z}$, the objective in (22) is concave in both $\hat{\Lambda}_s$ and $\hat{\Lambda}_b$. Hence, maximization can be computed efficiently using convex optimization algorithms.

2) Approximate ML Estimation via Censoring: We adapt the estimation via censoring in Section IV-B3 to the scenario in this section. Since z is known, the censoring estimator first extracts a cluster of signal detection times with a window of size t_{win} around the center of the pulse at time $t = 2z/c$. Then, it estimates Λ_b from the detection times outside of the signal cluster, and finally estimates Λ_s using detection times

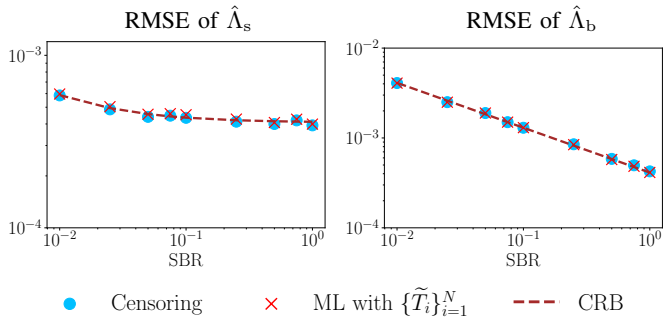

Fig. 3: RMSE of signal and background flux estimates when they are jointly estimated for known z. The mean number of signal photons is $n_\mathrm{r}\Lambda_\mathrm{s} = 6$. The "Censoring" points are estimates using the censoring approach (23) and (24). The "ML with $\{\widetilde{T}_i\}_{i=1}^N$" points are estimates which maximize the likelihood (12). "CRB" is the Cramér-Rao bound on the RMSE of $\hat{\Lambda}_\mathrm{s}$ and $\hat{\Lambda}_\mathrm{b}$ according to (26) and (27).

in the signal cluster.

$$\hat{\Lambda}_\mathrm{b} = \frac{N_\mathrm{b}}{n_\mathrm{r}} \frac{t_\mathrm{r}}{t_\mathrm{r} - t_\mathrm{win}} \tag{23}$$

$$\hat{\Lambda}_\mathrm{s} = \frac{N_\mathrm{s}}{n_\mathrm{r}} - \hat{\Lambda}_\mathrm{b} \frac{t_\mathrm{win}}{t_\mathrm{r}} \tag{24}$$

N_s is the size of the signal cluster, and $N_\mathrm{b} = N - N_\mathrm{s}$ is the number of detections outside the signal cluster.

3) Cramér-Rao Bound: The CRB lower bounds the covariance matrix of any unbiased estimator $[\hat{\Lambda}_\mathrm{s}\ \hat{\Lambda}_\mathrm{b}]^\top$ by the inverse of the Fisher information matrix about Λ_s and Λ_b:

$$\mathcal{I}\left(\Lambda_\mathrm{s}, \Lambda_\mathrm{b}\right) = -\mathbb{E}\begin{bmatrix} \frac{\partial^2 \log f}{\partial \Lambda_\mathrm{s}^2} & \frac{\partial^2 \log f}{\partial \Lambda_\mathrm{s} \partial \Lambda_\mathrm{b}} \\ \frac{\partial^2 \log f}{\partial \Lambda_\mathrm{s} \partial \Lambda_\mathrm{b}} & \frac{\partial^2 \log f}{\partial \Lambda_\mathrm{b}^2} \end{bmatrix}. \tag{25}$$

Each term in the matrix (25) is derived in Section A.

Since any positive semidefinite matrix has nonnegative diagonal entries, the MSE of $\hat{\Lambda}_\mathrm{s}$ and $\hat{\Lambda}_\mathrm{b}$ can be lower bounded:

$$\mathbb{E}\left[(\hat{\Lambda}_\mathrm{s} - \Lambda_\mathrm{s})^2\right] \geq \left[\mathcal{I}\left(\Lambda_\mathrm{s}, \Lambda_\mathrm{b}\right)^{-1}\right]_{11}; \tag{26}$$

$$\mathbb{E}\left[(\hat{\Lambda}_\mathrm{b} - \Lambda_\mathrm{b})^2\right] \geq \left[\mathcal{I}\left(\Lambda_\mathrm{s}, \Lambda_\mathrm{b}\right)^{-1}\right]_{22}. \tag{27}$$

4) Simulation Results: Some simulation results are shown in Figure 3. The ML estimator and the censoring estimator have approximately equal RMSE across SBR from 0.01 to 1.00 when the mean number of signal photons is $n_\mathrm{r}\Lambda_\mathrm{s} = 6$, and they both achieve the CRB.

V. High-Flux Reflectivity Estimation

When the total flux is sufficiently high (e.g., $\Lambda > 5\%$), the probability of a photon arriving during the dead time following a previous detection is significant, and the detection sequence can no longer be described as a Poisson process. As previously discussed, both SPADs and TCSPC electronics have dead times, and their particular reset strategies can significantly complicate the detection time modeling. Here we assume the SPAD has an asynchronous dead time with duration t_d, and the TCSPC electronics are asynchronous with dead time duration t_e. Table I lists manufacturer-specified dead times for common SPADs, and Table II lists dead times for asynchronous TCSPC electronics, showing significant variation in the dead time durations. In the following, we separately examine the case of $t_\mathrm{d} > t_\mathrm{e}$, when only the SPAD dead time needs to be considered, and the case of $t_\mathrm{d} < t_\mathrm{e}$, when both sources of dead time affect the detection sequence. Unlike the low-flux case, Fisher information analysis in the high-flux regime is still an open problem due to time-dependence of detections.

A. Flux Estimation with $t_\mathrm{d} > t_\mathrm{e}$

When $t_\mathrm{d} > t_\mathrm{e}$, the TCSPC electronics are always rearmed when the SPAD resets, so only the SPAD dead time needs to be considered. The probability of a photon being detected at a particular time T_{i+1} depends on both the photon arrival intensity and whether the SPAD is dead, i.e., at what time the previous photon T_i was detected. This dependence thus encourages the use of the absolute detection time sequence $\{T_i\}_{i=1}^N$. The conditional PDF of a detection at time T_{i+1} given all previous detection times is

$$\begin{aligned} &f_{T_{i+1}|T_1,T_2,\ldots,T_i}(t_{i+1}|t_1,\ldots,t_i) = f_{T_{i+1}|T_i}(t_{i+1}|t_i) \\ &= \begin{cases} \lambda(t_{i+1}) \exp\left(-\int_{t_i+t_\mathrm{d}}^{t_{i+1}} \lambda(\tau)\,\mathrm{d}\tau\right), & t_{i+1} > t_i + t_\mathrm{d} \\ 0, & \text{otherwise.} \end{cases} \end{aligned} \tag{28}$$

The fact that the conditional PDF depends only on the previous detection time T_i (and the intensity function $\lambda(t)$) makes the detection sequence a Markov chain, which has been exploited for depth estimation at high flux [16].

1) Background Flux Estimation for Calibration: As in the case of low-flux lidar, high-flux reflectivity estimation typically assumes a background calibration procedure to first estimate the background rate with the laser turned off. Despite the complication of dead times, background estimation is still fairly simple because λ_b is assumed to be constant. We follow the procedure outlined in [16]. Substituting λ_b for λ in (28), the conditional PDF of a background detection reduces to

$$\begin{aligned} &f_{T_{i+1}|T_i}(t_{i+1}|t_i) \\ &= \begin{cases} b \exp\{-b[t_{i+1} - (t_i + t_\mathrm{d})]\}, & t_{i+1} > t_i + t_\mathrm{d}, \\ 0, & \text{otherwise,} \end{cases} \end{aligned} \tag{29}$$

which shows that, after the dead time, the probability of the next detection time is a shifted exponential random variable. Note that it may be unknown whether the detector is dead at the start of data collection, which would affect the distibution of the first detection time. Hence conditioning on the first detection time T_1, we use the property that the detection sequence is a Markov chain to get the joint PDF of the entire detection sequence

$$f_{T_2,\ldots,T_N|T_1}(t_2,\ldots,t_N|t_1) = \prod_{i=1}^{N-1} f_{T_{i+1}|T_i}(t_{i+1}|t_i) \tag{30}$$

$$= b^{N-1} \exp[-b(t_N - t_1) + (N-1)bt_\mathrm{d}]. \tag{31}$$

We observe that (31) resembles a modified Erlang$(N-1, b)$ random variable that sums the $N-1$ exponential inter-detection times and subtracts the known total dead time

TABLE I: Manufacturer-specified dead times for some common visible-wavelength SPADs (sources:[82], [83], [84], [85])

Manufacturer	Product Name	Dead time [ns]
Excelitas	SPCM-AQRH-1X	22
ID Quantique	ID100-50-STD	45
Thorlabs	SPDMH2	45
PicoQuant (MPD)	PDM	77

TABLE II: Manufacturer-specified dead times for some common TCSPC electronics (sources: [86], [87], [88]).

Manufacturer	Model	Dead Time [ns]
PicoQuant	MultiHarp 150P	0.65
Swabian Instruments	Time Tagger X	1.5
Swabian Instruments	Time Tagger Ultra	2.1
Swabian Instruments	Time Tagger 20	6
PicoQuant	TimeHarp 260P	25
quTools	quTAG	40
PicoQuant	HydraHarp 400	80
PicoQuant	PicoHarp 300	95

$(N-1)t_{\mathrm{d}}$. Estimating b is thus fairly straightforward. Given the absolute detection times $\{T_i\}_{i=1}^N$, the conditional log-likelihood is

$$\begin{aligned}&\mathcal{L}\big(\{T_i\}_{i=1}^N; b\big)\\ &\quad = (N-1)\ln(b) - b(T_N - T_1) + (N-1)bt_{\mathrm{d}}.\end{aligned} \tag{32}$$

Differentiating (32) with respect to b and setting the derivative equal to zero yields the conditional ML estimator

$$\hat{b} = \frac{N-1}{(T_N - T_1) - (N-1)t_{\mathrm{d}}}. \tag{33}$$

It is noteworthy that the background flux estimate is based not only on the detection count N, but also on the detection times T_1 and T_N. However, not all photon times need to be stored to perform the estimate—only the first and last detections are needed. Storing high-resolution time stamps for the entire detection sequence can be memory intensive for large N, but for background calibration, storing each detection time is unnecessary. Instead, it is possible to retain only the first and last detection times, which could be integrated into digital memory of the detector circuitry itself.

2) Background Flux Estimation for Passive Imaging: Although the main focus of this paper is on active reflectivity imaging, similar modeling is useful for passive imaging as well. Several recent works have considered passive imaging with time-resolved single-photon focal-plane arrays [89], [18], [90]. Since existing SPAD arrays tend to have limited pixel count and/or timing resolution, a SPAD array with high spatial and temporal resolution was emulated with a single-pixel SPAD mechanically scanned around the focal plane of a lens. Each position of the SPAD was collimated to collect light from only one point in the scene. Without an active illumination source, the only variation in the flux reaching the SPAD was due to the changes in scene reflectivity, reflecting ambient light towards the focused SPAD. Scene reflectivity estimation then becomes a flux estimation problem.

Initial work used only the photon counts N for estimation [89]. Since the background estimator without dead times is the detection count N scaled by the exposure time t_{exp}, the estimator was modified to remove dead times, i.e.,

$$\hat{b}^{\mathrm{PF-SPAD}} = \frac{N}{t_{\mathrm{exp}} - Nt_{\mathrm{d}}}. \tag{34}$$

Later work recognized that at very high flux, the total *number* of detected photons has very low variance, whereas the detection times retain more nuanced information [18]. As a result, a refined estimator was proposed identical to (33). Using photon count statistics, especially with the detection times, has much larger dynamic range than conventional cameras, which rely on varying exposure times (i.e., "exposure bracketing" [91]) to capture both low- and high-flux scene components in the same image. Single-photon detection can thus natively achieve high dynamic-range (HDR) imaging, or can be combined with conventional cameras to guide exposure bracketing [90].

3) Signal Flux Estimation with $t_{\mathrm{d}} > t_{\mathrm{e}}$: Ideally, reflectivity estimation in active illumination settings (i.e., single-photon lidar) would follow a similar method as in background calibration. The joint PDF for the sequence of N detections $\{T_i\}_{i=1}^N$, conditioned on T_1 is

$$\begin{aligned}f_{T_2,\ldots,T_n|T_1}(t_2,\ldots,t_N|t_1) &= \prod_{i=1}^{n-1} f_{T_{i+1}|T_i}(t_{i+1}|t_i)\\ &= \prod_{i=1}^{n-1}\left[\lambda(t_{i+1})\exp\left(-\int_{t_i+t_{\mathrm{d}}}^{t_{i+1}}\lambda(t)\,\mathrm{d}t\right)\right]\\ &= \left(\prod_{i=2}^{n}\widetilde{\lambda}(\tilde{t}_i)\right)\exp\left(-\int_{\mathcal{T}}\lambda(t)\,\mathrm{d}t\right),\end{aligned} \tag{35}$$

where $\mathcal{T} = \bigcup_{i=1}^{n-1}[t_i + t_{\mathrm{d}}, t_{i+1}]$. The log-likelihood is

$$\begin{aligned}&\log f_{T_2,\ldots,T_n|T_1}(t_2,\ldots,t_n|t_1)\\ &\quad = \sum_{i=2}^{n}\log\left(\Lambda_{\mathrm{s}}s(\tilde{t}_i - 2z/c) + b\right) - b\,|\mathcal{T}|\\ &\qquad - \Lambda_{\mathrm{s}}\int_{\mathcal{T}}\left(\sum_{k=0}^{n_{\mathrm{r}}-1}s(t - 2z/c - kt_{\mathrm{r}})\right)\mathrm{d}t\,,\end{aligned} \tag{36}$$

which is concave in Λ_{s} and b but nonconcave in z, similar to the maximization objective in (15). If z is known, maximizing the likelihood with respect to Λ_{s} and b is easy, but z is usually unknown in lidar settings. Furthermore, existing depth estimators that account for dead time often themselves rely on having an accurate reflectivity estimate [16], [17]. Similar to the case without dead time (15), a brute force search for joint ML estimation of both Λ_{s} and z is possible but impractical.

An alternative method for estimating the reflectivity independent of the depth was proposed in [16] by relying on the periodicity of the arrival intensity $\lambda(t)$. Since the total flux in each period Λ is independent of z, combining the total flux and background calibration estimates produces a signal flux estimate $\hat{\Lambda}_{\mathrm{s}} = \max(0, \hat{\Lambda} - \hat{b}t_{\mathrm{r}})$. Instead of keeping track of the amount of time between photon detections, one can instead keep track of the number of illumination cycles between detections. Define the inter-detection time as $U_i = T_{i+1} - T_i,\ i = 1,\ldots,N-1$. Then the number of *inter-detection periods* is defined as $R_i = \lfloor (U_i - t_{\mathrm{d}})/t_{\mathrm{r}} \rfloor$, which

counts the number of periods after the dead time following T_i before the next photon is detected at T_{i+1}. Note that R_i is distinct from the difference of illumination period indices $M_{i+1} - M_i$, which does not account for dead time.

Because the photon arrival process is Poisson with rate Λ, the probability of zero photons arriving in a particular period is $\exp(-\Lambda)$, and the probability of one or more photons arriving in that period is $q = 1 - \exp(-\Lambda)$. We thus consider each inter-detection period to be a Bernoulli random variable with probability q that one or more photons was detected. The number of periods until a photon is detected is a geometric random variable with probability mass function (PMF)

$$P(R_i = r_i) = (1-q)^{r_i} q, \;\; r_i = 0, 1, \ldots. \tag{37}$$

Given N photon detections, there are $N-1$ independent inter-detection periods, so their joint probabilty is

$$p\big(\{R_i\}_{i=1}^{N-1}; \Lambda\big) = \prod_{i=1}^{N-1} [1 - \exp(-\Lambda)] \exp(-R_i \Lambda) \tag{38}$$

and the log-likelihood is

$$\mathcal{L}\big(\{R_i\}_{i=1}^{N-1}; \Lambda\big) = -\Lambda \sum_{i=1}^{N-1} R_i + N \log[1 - \exp(-\Lambda)]. \tag{39}$$

Differentiating the log-likelihood with respect to Λ and setting the derivative to zero yields the total flux ML estimator

$$\hat{\Lambda} = \log\left(1 + \frac{N-1}{\sum_{i=1}^{N-1} R_i}\right). \tag{40}$$

Once again, the total flux estimator uses not only the photon detection count N but also the detection times, embedded in the calculation of the inter-detection periods. Moreover, the individual times do not need to be stored—only a running sum of the inter-detection periods is needed, as well as a tally of the number of detections—which could aid in on-chip processing. One downside of this approach is the dynamic range is limited by the floor function, which retains only the number of periods and not the exact times between detections. As Λ increases, the probability of observing $R_i > 0$ decreases, so the estimator saturates as seen in Fig. 4. When detections occur often enough, we may observe $R_i = 0$ for all $i = 1, \ldots, N-1$. We define $\hat{\Lambda} = +\infty$ in this case. Consequently, the bias of estimator (40) is $+\infty$, because such observation has a positive probability. Further research on more sophisticated and robust estimators that use the raw detection times themselves is warranted.

B. Flux Estimation with $t_\mathrm{d} < t_\mathrm{e}$

Most work on single-photon lidar considers only the detector as a source of dead time—if at all—because when $t_\mathrm{d} > t_\mathrm{e}$, the electronics are always armed and ready to record a photon before the detector has reset, so t_e can be ignored. However, as illustrated by the values for t_d in Table I and t_e in Table II, it is easy to construct a configuration in which $t_\mathrm{d} < t_\mathrm{e}$.

We briefly consider a lidar system with $t_\mathrm{d} < t_\mathrm{e}$ with both the detector and electronics reset when a photon arrives at time T_i. The photon is detected and registered by both

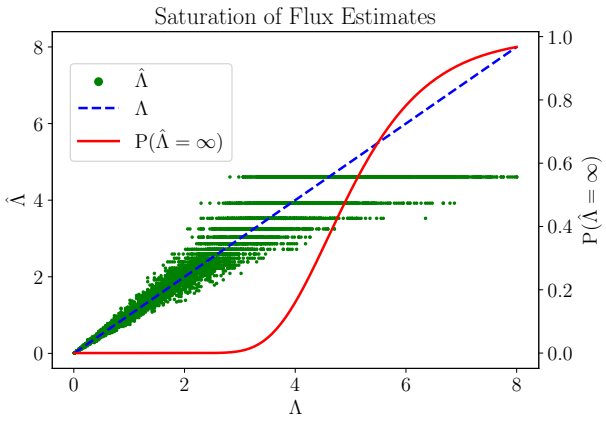

Fig. 4: Flux estimates based on inter-detection periods $\{R_i\}_{i=1}^{N-1}$ saturate as the probability of observing $R > 0$ decreases with increasing Λ. The green points show 50 realizations each of flux estimates with $N = 100$ for $\Lambda \in [0, 8]$. The probability that the estimate saturates is $P(\hat{\Lambda} = \infty) = P(\sum_{i=1}^{N-1} R_i = 0) = (1 - \exp(-\Lambda))^{N-1}$ shown in red.

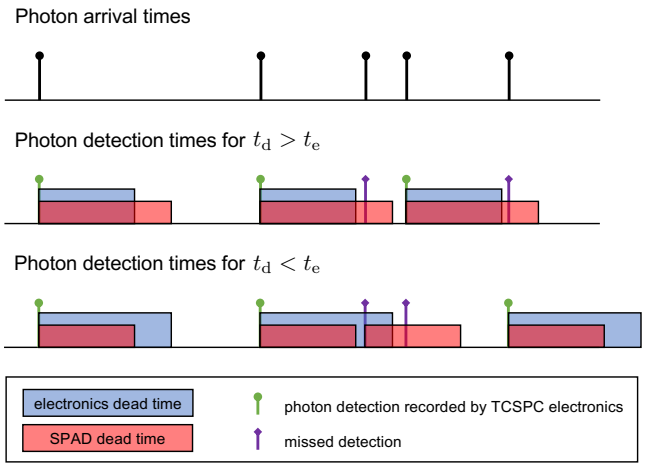

Fig. 5: Not all photons arriving at the SPAD detector can be time-stamped by the TCSPC electronics. When $t_\mathrm{d} > t_\mathrm{e}$, only the detector dead time determines which photons are recorded and which are missed. When $t_\mathrm{d} < t_\mathrm{e}$, both sources of dead time influence the photon detection sequence.

devices, and both the detector and electronics are subsequently dead. At $T_i + t_\mathrm{d}$, the detector has reset and is sensitive to arriving photons. However, until $T_i + t_\mathrm{e}$, the electronics are still insensitive. If a photon arrives at time $Y_i \in (T_i + t_\mathrm{d}, T_i + t_\mathrm{e})$, the detector will detect the photon and go dead, but the electronics will not register the detection. The electronics will once again be sensitive at $T_i + t_\mathrm{e}$, but the detector may still be dead if $Y_i + t_\mathrm{d} > T_i + t_\mathrm{e}$. Now the entire duration that the system is dead depends on an unobserved photon at time Y_i. The differences in the detection time sequences for $t_\mathrm{d} > t_\mathrm{e}$ and $t_\mathrm{d} < t_\mathrm{e}$ are illustrated in Fig. 5.

Because of the complexities of having multiple sources of dead time, the following analysis is restricted to $t_\mathrm{r}/2 \leq t_\mathrm{d} \leq$

$t_\mathrm{e} \le t_\mathrm{r}$ as discussed in [17]. Like the case of $t_\mathrm{d} > t_\mathrm{e}$, the conditional PDF of the detection times is still found to yield a Markov Chain detection sequence with transition probability

$$f_{T_{i+1}|T_i}(t_{i+1}|t_i) = g(t_i, t_{i+1}) \Bigg[\mathbb{I}\{t_{i+1} > t_i + t_\mathrm{e}\} + \int_{t_i+t_\mathrm{d}}^{t_{i+1}-t_\mathrm{d}} h(y)\ \mathrm{d}y\ \mathbb{I}\{t_i + 2t_\mathrm{d} < t_{i+1} \le t_i + t_\mathrm{d} + t_\mathrm{e}\} + \int_{t_i+t_\mathrm{d}}^{t_i+t_\mathrm{e}} h(y)\ \mathrm{d}y\ \mathbb{I}\{t_{i+1} > t_i + t_\mathrm{d} + t_\mathrm{e}\} \Bigg], \tag{41a}$$

where

$$g(t_i, t_{i+1}) = \lambda(t_{i+1}) \exp\left(- \int_{t_i+t_\mathrm{d}}^{t_{i+1}} \lambda(\tau)\ \mathrm{d}\tau \right), \tag{41b}$$

$$h(y) = \lambda(y) \exp\left(\int_{y}^{y+t_\mathrm{d}} \lambda(\tau)\ \mathrm{d}\tau \right), \tag{41c}$$

but the PDF (41) is obviously more complicated than (28).

As in the case of $t_\mathrm{d} > t_\mathrm{e}$, the inter-detection time is defined as $U_i = T_{i+1} - T_i,\ i = 1, \ldots, N-1$. However, the possibility of an unobserved photon means the inter-detection times could have varying and unknown dead times. Thus only the subsequence of the inter-detection times $(U_{i_k})_k$ for which $U_{i_k} \ge t_\mathrm{d} + t_\mathrm{e}$ has well-defined statistics. The number of "inter-detection periods" is modified to $R_i = \lfloor (U_i - t_\mathrm{d} - t_\mathrm{e})/t_\mathrm{r} \rfloor$, which counts the number of periods after both dead times following T_i before the next photon is detected at T_{i+1}. By using only the constrained sub-sequence of detections, the inter-detection periods once again have a geometric distribution, so the same ML estimator of the total flux in (40) applies.

A downside of relying on the constrained sub-sequence is that not all inter-detection periods can be used. In fact, the number of useful inter-detection periods decreases as the flux increases, and the number of useful inter-detection periods with $R_i > 0$ is even smaller, decreasing the accuracy of the flux estimator. A further limitation is that background calibration must also use the estimator in (40) based on sub-sequences, so both background and total flux estimation are less accurate when $t_\mathrm{e} > t_\mathrm{d}$.

VI. Conclusions

Accurate reflectivity estimation is often considered secondary to depth estimation with lidar. However, reflectivity can provide useful information about material properties (e.g., in hyperspectral lidar), assist in the fusing of multiple modalities (e.g., lidar and cameras), or be used for prior information about scene structure in depth estimation tasks. While many works incorporate spatial redundancy to regularize reflectivity estimates, in this paper we focused on how much information about the signal flux (a linear scaling of reflectivity) can be extracted from a single pointwise measurement with single-photon lidar. Perhaps surprisingly, not only the number of photon detections but also the detection times contain flux information. A persistent challenge of using the detection times is that the maximum likelihood estimate of the flux is usually coupled to the depth. Although brute-force search over both parameters can lead to good estimates, the approach is usually impractical. Instead, we re-evaluate several existing methods that perform flux estimation without first estimating the depth. We also add context for whether the absolute detection times are needed, whether relative detection times modulo the illumination period will suffice, or whether other functions of the absolute times can be computed on-chip with reduced memory requirements.

In high-flux conditions, when dead time cannot be ignored, the particular SPL hardware architecture affects the detection time model and the resulting flux estimators. Jointly estimating reflectivity and depth—especially in the presence of dead times and with different architectures—warrants further investigation. Future work could also consider lower bounds on the estimation accuracy in the presence of dead times. Another interesting problem would be to consider co-axial systems that have reflectivity information in both the active measurement (lidar) and passive measurement (background calibration).

Appendix A
Fisher Information for Low-Flux Estimation

We will derive the Fisher information matrix about Λ_s, Λ_b, and z in the number of detections N and the relative detection times $\{\widetilde{T}_i\}_{i=1}^N$ for the low-flux detection model. The Fisher information matrix is

$$\mathcal{I}\left(\Lambda_\mathrm{s}, \Lambda_\mathrm{b}, z\right) = -\mathbb{E}\begin{bmatrix} \frac{\partial^2 \log f}{\partial \Lambda_\mathrm{s}^2} & \frac{\partial^2 \log f}{\partial \Lambda_\mathrm{s} \partial \Lambda_\mathrm{b}} & \frac{\partial^2 \log f}{\partial \Lambda_\mathrm{s} \partial z} \\ \frac{\partial^2 \log f}{\partial \Lambda_\mathrm{s} \partial \Lambda_\mathrm{b}} & \frac{\partial^2 \log f}{\partial \Lambda_\mathrm{b}^2} & \frac{\partial^2 \log f}{\partial \Lambda_\mathrm{b} \partial z} \\ \frac{\partial^2 \log f}{\partial \Lambda_\mathrm{s} \partial z} & \frac{\partial^2 \log f}{\partial \Lambda_\mathrm{b} \partial z} & \frac{\partial^2 \log f}{\partial z^2} \end{bmatrix}, \tag{42}$$

where $f := f_{N, \widetilde{T}_1, \ldots, \widetilde{T}_N}(N, \widetilde{T}_1, \ldots, \widetilde{T}_n)$ is the distribution (12). By the CRB, the covariance matrix of an unbiased estimate $[\hat{\Lambda}_\mathrm{s}\ \hat{\Lambda}_\mathrm{b}\ \hat{z}]^\top$ is lower bounded by $\mathcal{I}\left(\Lambda_\mathrm{s}, \Lambda_\mathrm{b}, z\right)^{-1}$.

To simplify the expressions that will follow, we introduce the following notation:

$$\begin{aligned} s_i &:= s(\widetilde{T}_i - 2z/c); \\ s_i' &:= s'(\widetilde{T}_i - 2z/c), \text{ where } s'(t) = \frac{\mathrm{d}s(t)}{\mathrm{d}t}; \\ s_i'' &:= s''(\widetilde{T}_i - 2z/c), \text{ where } s''(t) = \frac{\mathrm{d}^2 s(t)}{\mathrm{d}t^2}; \\ \widetilde{\lambda}_i &:= \widetilde{\lambda}(\widetilde{T}_i) = \Lambda_\mathrm{s} s(\widetilde{T}_i - 2z/c) + \Lambda_\mathrm{b}/t_\mathrm{r}. \end{aligned}$$

We calculate the first derivatives:

$$\begin{aligned} \frac{\partial}{\partial \Lambda_\mathrm{s}} \log f &= -n_\mathrm{r} + \sum_{i=1}^N \frac{s_i}{\widetilde{\lambda}_i} \\ \frac{\partial}{\partial \Lambda_\mathrm{b}} \log f &= -n_\mathrm{r} + \sum_{i=1}^N \frac{1/t_\mathrm{r}}{\widetilde{\lambda}_i} \\ \frac{\partial}{\partial z} \log f &= -\frac{2\Lambda_\mathrm{s}}{c} \sum_{i=1}^N \frac{s_i'}{\widetilde{\lambda}_i} \end{aligned}$$

Then, we calculate the expected value of the second derivatives. We use the fact that the measurement $\{\widetilde{T}_i\}_{i=1}^N$ implies the number of detections N, so $\widetilde{T}_1, \ldots, \widetilde{T}_N$ and N are mutually independent. Therefore, $\mathbb{E}\sum_{i=1}^N g(\widetilde{T}_i) = \mathbb{E}\left[N\right] \mathbb{E}[g(\widetilde{T}_1)]$

for any function g. All terms in the Fisher information matrix (42) can be simplified with this identity:

$$\mathbb{E}\frac{\partial^2}{\partial\Lambda_{\mathrm{s}}^2}\log f = -n_{\mathrm{r}}\Lambda\mathbb{E}\left[\left(\frac{s_1}{\widetilde{\lambda}_1}\right)^2\right]$$

$$\mathbb{E}\frac{\partial^2}{\partial\Lambda_{\mathrm{b}}^2}\log f = -\frac{n_{\mathrm{r}}\Lambda}{t_{\mathrm{r}}^2}\mathbb{E}\left[\left(\frac{1}{\widetilde{\lambda}_1}\right)^2\right]$$

$$\mathbb{E}\frac{\partial^2}{\partial z^2}\log f = n_{\mathrm{r}}\Lambda\left(\frac{2\Lambda_{\mathrm{s}}}{c}\right)^2\mathbb{E}\left[\frac{s_1''}{\Lambda_{\mathrm{s}}\widetilde{\lambda}_1} - \left(\frac{s_1'}{\widetilde{\lambda}_1}\right)^2\right]$$

$$\mathbb{E}\frac{\partial^2}{\partial\Lambda_{\mathrm{s}}\partial\Lambda_{\mathrm{b}}}\log f = -\frac{n_{\mathrm{r}}\Lambda}{t_{\mathrm{r}}}\mathbb{E}\left[\frac{s_1}{\widetilde{\lambda}_1^2}\right]$$

$$\mathbb{E}\frac{\partial^2}{\partial\Lambda_{\mathrm{s}}\partial z}\log f = \frac{2n_{\mathrm{r}}\Lambda}{c}\mathbb{E}\left[\Lambda_{\mathrm{s}}\frac{s_1's_1}{\widetilde{\lambda}_1^2} - \frac{s_1'}{\widetilde{\lambda}_1}\right]$$

$$\mathbb{E}\frac{\partial^2}{\partial\Lambda_{\mathrm{b}}\partial z}\log f = n_{\mathrm{r}}\Lambda\frac{2\Lambda_{\mathrm{s}}}{ct_{\mathrm{r}}}\mathbb{E}\left[\frac{s_i'}{\widetilde{\lambda}_i^2}\right]$$

We note that $\mathbb{E}[\partial^2 f/\partial\Lambda_{\mathrm{s}}\partial z]$ and $\mathbb{E}[\partial^2 f/\partial\Lambda_{\mathrm{b}}\partial z]$ are approximately zero when the pulse shape $s(t)$ is symmetric and the FWHM pulse width is very short in comparison to the repetition period t_{r}.

REFERENCES

[1] J. Ring, "The laser in astronomy," *New Scientist*, vol. 18, pp. 672–673, 20 June 1963.

[2] H. Wang, C. Wang, and L. Xie, "Intensity scan context: Coding intensity and geometry relations for loop closure detection," in *2020 IEEE Int. Conf. Robot. Autom.*, pp. 2095–2101, 2020.

[3] Y. Zhang, Y. Tian, W. Wang, G. Yang, Z. Li, F. Jing, and M. Tan, "RI-LIO: Reflectivity image assisted tightly-coupled LiDAR-inertial odometry," *IEEE Robot. Autom. Lett.*, vol. 8, no. 3, pp. 1802–1809, 2023.

[4] T. Yin, J. Yao, Y. Lu, and C. Na, "Solid-state-lidar-inertial-visual odometry and mapping via quadratic motion model and reflectivity information," *J. Electron.*, vol. 12, no. 17, 2023.

[5] Y. Chen, C. Jiang, J. Hyyppä, S. Qiu, Z. Wang, M. Tian, W. Li, E. Puttonen, H. Zhou, Z. Feng, Y. Bo, and Z. Wen, "Feasibility study of ore classification using active hyperspectral LiDAR," *IEEE Geosci. Remote Sens. Lett.*, vol. 15, no. 11, pp. 1785–1789, 2018.

[6] H. Shao, Y. Chen, Z. Yang, C. Jiang, W. Li, H. Wu, Z. Wen, S. Wang, E. Puttnon, and J. Hyyppä, "A 91-channel hyperspectral LiDAR for coal/rock classification," *IEEE Geosci. Remote Sens. Lett.*, vol. 17, no. 6, pp. 1052–1056, 2020.

[7] B. Wang, J. Liu, J. Li, and M. Li, "UAV LiDAR and hyperspectral data synergy for tree species classification in the Maoershan forest farm region," *Remote Sens.*, vol. 15, no. 4, 2023.

[8] A. Kirmani, D. Venkatraman, D. Shin, A. Colaço, F. N. C. Wong, J. H. Shapiro, and V. K. Goyal, "First-photon imaging," *Science*, vol. 343, no. 6166, pp. 58–61, 2014.

[9] D. Shin, A. Kirmani, V. K. Goyal, and J. H. Shapiro, "Photon-efficient computational 3D and reflectivity imaging with single-photon detectors," *IEEE Trans. Comput. Imaging*, vol. 1, pp. 112–125, June 2015.

[10] Y. Altmann, X. Ren, A. McCarthy, G. S. Buller, and S. McLaughlin, "Lidar waveform-based analysis of depth images constructed using sparse single-photon data," *IEEE Trans. Image Process.*, vol. 25, pp. 1935–1946, May 2016.

[11] Y. Altmann, X. Ren, A. McCarthy, G. S. Buller, and S. McLaughlin, "Robust Bayesian target detection algorithm for depth imaging from sparse single-photon data," *IEEE Trans. Comput. Imaging*, vol. 2, pp. 456–467, Dec. 2016.

[12] J. Tachella, Y. Altmann, X. Ren, A. McCarthy, G. S. Buller, S. McLaughlin, and J.-Y. Tourneret, "Bayesian 3D reconstruction of complex scenes from single-photon lidar data," *SIAM J. Imaging Sci.*, vol. 12, pp. 521–550, Jan. 2019.

[13] J. Rapp and V. K. Goyal, "A few photons among many: Unmixing signal and noise for photon-efficient active imaging," *IEEE Trans. Comput. Imaging*, vol. 3, no. 3, pp. 445–459, 2017.

[14] D. B. Lindell, M. O'Toole, and G. Wetzstein, "Single-photon 3D imaging with deep sensor fusion," *ACM Trans. Graph.*, vol. 37, no. 4, p. 113, 2018.

[15] J. Lee, A. Ingle, J. V. Chacko, K. W. Eliceiri, and M. Gupta, "CASPI: collaborative photon processing for active single-photon imaging," *Nature Commun.*, vol. 14, p. 3158, May 2023.

[16] J. Rapp, Y. Ma, R. M. A. Dawson, and V. K. Goyal, "Dead time compensation for high-flux ranging," *IEEE Trans. Signal Process.*, pp. 3471–3486, Oct. 2019.

[17] J. Rapp, Y. Ma, R. M. A. Dawson, and V. K. Goyal, "High-flux single-photon lidar," *Optica*, vol. 8, pp. 30–39, Nov. 2021.

[18] A. Ingle, T. Seets, M. Buttafava, S. Gupta, A. Tosi, M. Gupta, and A. Velten, "Passive inter-photon imaging," in *Proc. IEEE Conf. Comput. Vis. Pattern Recog.*, pp. 8581–8591, 2021.

[19] R. M. Marino, R. M. Spitzberg, and M. J. Bohrer, "A photon counting 3-D imaging laser radar for advanced discriminating interceptor seekers," in *2nd Ann. AIAA SDIO Interceptor Technology Conf.*, June 1993.

[20] B. F. Aull, A. H. Loomis, J. A. Gregory, and D. J. Young, "Geiger-mode avalanche photodiode arrays integrated with CMOS timing circuits," in *56th Ann. Device Research Conf. Dig.*, pp. 58–59, June 1983.

[21] B. F. Aull, A. H. Loomis, D. J. Young, R. M. Heinrichs, B. J. Felton, P. J. Daniels, and D. J. Landers, "Geiger-mode avalanche photodiodes for three-dimensional imaging," *Lincoln Lab. J.*, vol. 13, no. 2, pp. 335–350, 2002.

[22] M. A. Albota, B. F. Aull, D. G. Fouche, R. M. Heinrichs, D. G. Kocher, R. M. Marino, J. G. Mooney, N. R. Newbury, M. E. O'Brien, B. E. Player, B. C. Willard, and J. J. Zayhowski, "Three-dimensional imaging laser radars with Geiger-mode avalanche photodiode arrays," *Lincoln Lab. J.*, vol. 13, no. 2, pp. 351–370, 2002.

[23] M. A. Albota, R. M. Heinrichs, D. G. Kocher, D. G. Fouche, B. E. Player, M. E. O'Brien, B. F. Aull, J. J. Zayhowski, J. Mooney, B. C. Willard, and R. R. Carlson, "Three-dimensional imaging laser radar with a photon-counting avalanche photodiode array and microchip laser," *Appl. Optics*, vol. 41, no. 36, pp. 7671–7678, 2002.

[24] J. S. Massa, A. M. Wallace, G. S. Buller, S. J. Fancey, and A. C. Walker, "Laser depth measurement based on time-correlated single-photon counting," *Opt. Lett.*, vol. 22, no. 8, pp. 543–545, 1997.

[25] J. S. Massa, G. S. Buller, A. C. Walker, S. Cova, M. Umasuthan, and A. M. Wallace, "Time-of-flight optical ranging system based on time-correlated single-photon counting," *Appl. Optics*, vol. 37, no. 31, pp. 7298–7304, 1998.

[26] G. Buller and A. Wallace, "Ranging and three-dimensional imaging using time-correlated single-photon counting and point-by-point acquisition," *IEEE J. Sel. Top. Quantum Electron.*, vol. 13, pp. 1006–1015, July–Aug. 2007.

[27] A. McCarthy, R. J. Collins, N. J. Krichel, V. Fernández, A. M. Wallace, and G. S. Buller, "Long-range time-of-flight scanning sensor based on high-speed time-correlated single-photon counting," *Appl. Optics*, vol. 48, pp. 6241–6251, Nov. 2009.

[28] A. McCarthy, N. J. Krichel, N. R. Gemmell, X. Ren, M. G. Tanner, S. N. Dorenbos, V. Zwiller, R. H. Hadfield, and G. S. Buller, "Kilometer-range, high resolution depth imaging via 1560 nm wavelength single-photon detection," *Opt. Express*, vol. 21, pp. 8904–8915, Apr. 2013.

[29] A. McCarthy, X. Ren, A. Della Frera, N. R. Gemmell, N. J. Krichel, C. Scarcella, A. Ruggeri, A. Tosi, and G. S. Buller, "Kilometer-range depth imaging at 1550 nm wavelength using an InGaAs/InP single-photon avalanche diode detector," *Opt. Express*, vol. 21, pp. 22098–22113, Sept. 2013.

[30] D. Shin, F. Xu, D. Venkatraman, R. Lussana, F. Villa, F. Zappa, V. K. Goyal, F. N. C. Wong, and J. H. Shapiro, "Photon-efficient imaging with a single-photon camera," *Nat. Commun.*, vol. 7, 24 June 2016.

[31] D. Shin, J. H. Shapiro, and V. K. Goyal, "Single-photon depth imaging using a union-of-subspaces model," *IEEE Signal Process. Lett.*, vol. 22, pp. 2254–2258, Dec. 2015.

[32] Z. Sun, D. Lindell, O. Solgaard, and G. Wetzstein, "SPADnet: Deep RGB-SPAD sensor fusion assisted by monocular depth estimation," *Opt. Expr.*, vol. 28, pp. 14948–14962, Apr. 2020.

[33] J. Peng, Z. Xiong, X. Huang, Z.-P. Li, D. Liu, and F. Xu, "Photon-efficient 3D imaging with a non-local neural network," in *Proc. Eur. Conf. Comput. Vis.*, vol. 12374, (Cham), pp. 225–241, Springer International Publishing, 2020.

[34] A. M. Pawlikowska, A. Halimi, R. A. Lamb, and G. S. Buller, "Single-photon three-dimensional imaging at up to 10 kilometers range," *Opt. Express*, vol. 25, no. 10, pp. 11919–11931, 2017.

[35] Z.-P. Li, X. Huang, Y. Cao, B. Wang, Y.-H. Li, W. Jin, C. Yu, J. Zhang, Q. Zhang, C.-Z. Peng, F. Xu, and J.-W. Pan, "Single-photon computational 3D imaging at 45 km," *Photonics Res.*, vol. 8, pp. 1532–1540, Apr. 2020.

[36] Z.-P. Li, J. Ye, X. Huang, P.-Y. Jiang, Y. Cao, Y. Hong, C. Yu, J. Zhang, Q. Zhang, C.-Z. Peng, F. Xu, and J.-W. Pan, "Single-photon imaging over 200 km," *Optica*, vol. 8, pp. 344–349, Jan. 2021.

[37] A. Maccarone, A. McCarthy, X. Ren, R. E. Warburton, A. M. Wallace, J. Moffat, Y. Petillot, and G. S. Buller, "Underwater depth imaging using time-correlated single-photon counting," *Opt. Express*, vol. 23, pp. 33911–33926, Dec. 2015.

[38] G. Satat, M. Tancik, and R. Raskar, "Towards photography through realistic fog," in *Proc. IEEE Int. Conf. Comput. Photography*, pp. 1–10, May 2018.

[39] R. Tobin, A. Halimi, A. McCarthy, M. Laurenzis, F. Christnacher, and G. S. Buller, "Three-dimensional single-photon imaging through obscurants," *Opt. Express*, vol. 27, pp. 4590–4611, Feb. 2019.

[40] D. Shin, F. Xu, F. N. C. Wong, J. H. Shapiro, and V. K. Goyal, "Computational multi-depth single-photon imaging," *Opt. Express*, vol. 24, pp. 1873–1888, Feb. 2016.

[41] A. Halimi, R. Tobin, A. McCarthy, S. McLaughlin, and G. S. Buller, "Restoration of multilayered single-photon 3D lidar images," in *Proc. Eur. Signal Proc. Conf.*, pp. 708–712, Aug. 2017.

[42] A. Halimi, R. Tobin, A. McCarthy, J. M. Bioucas-Dias, S. McLaughlin, and G. S. Buller, "Robust restoration of sparse multidimensional single-photon LiDAR images," *IEEE Trans. Comput. Imaging*, pp. 1–1, 2019.

[43] J. Tachella, Y. Altmann, N. Mellado, A. McCarthy, R. Tobin, G. S. Buller, J.-Y. Tourneret, and S. McLaughlin, "Real-time 3D reconstruction from single-photon lidar data using plug-and-play point cloud denoisers," *Nat. Commun.*, vol. 10, p. 4984, Nov. 2019.

[44] S. Plosz, A. Maccarone, S. McLaughlin, G. S. Buller, and A. Halimi, "Real-time reconstruction of 3d videos from single-photon lidar data in the presence of obscurants," *IEEE Trans. Comput. Imaging*, vol. 9, pp. 106–119, 2023.

[45] Y. Altmann, S. McLaughlin, and M. E. Davies, "Fast online 3d reconstruction of dynamic scenes from individual single-photon detection events," *IEEE Trans. Image Process.*, vol. 29, pp. 2666–2675, 2020.

[46] Z. Li, J. Lai, C. Wang, W. Yan, and Z. Li, "Influence of dead-time on detection efficiency and range performance of photon-counting laser radar that uses a Geiger-mode avalanche photodiode," *Appl. Optics*, vol. 56, pp. 6680–6687, Aug. 2017.

[47] F. Heide, S. Diamond, D. B. Lindell, and G. Wetzstein, "Sub-picosecond photon-efficient 3D imaging using single-photon sensors," *Sci. Rep.*, vol. 8, p. 17726, Dec. 2018.

[48] A. K. Pediredla, A. C. Sankaranarayanan, M. Buttafava, A. Tosi, and A. Veeraraghavan, "Signal processing based pile-up compensation for gated single-photon avalanche diodes." arXiv:1806.07437, June 2018.

[49] R. A. Barton-Grimley, J. P. Thayer, and M. Hayman, "Nonlinear target count rate estimation in single-photon lidar due to first photon bias," *Opt. Lett.*, vol. 44, pp. 1249–1252, Mar. 2019.

[50] A. Gupta, A. Ingle, A. Velten, and M. Gupta, "Photon-flooded single-photon 3D cameras," in *Proc. IEEE Conf. Comput. Vis. Pattern Recog.*, pp. 6770–6779, June 2019.

[51] A. Gupta, A. Ingle, and M. Gupta, "Asynchronous single-photon 3D imaging," in *Proc. IEEE Int. Conf. Comput. Vis.*, pp. 7908–7917, 2019.

[52] Z. Li, J. Lai, Z. Wu, C. Wang, W. Yan, and Z. Li, "Dead-time-based sequence coding method for single-photon lidar ranging," *Opt. Commun.*, vol. 517, p. 128260, Aug. 2022.

[53] A. Raghuram, A. Pediredla, S. G. Narasimhan, I. Gkioulekas, and A. Veeraraghavan, "STORM: Super-resolving Transients by OveRsampled Measurements," in *Proc. IEEE Int. Conf. Comput. Photog.*, pp. 44–54, 2019.

[54] J. Rapp, R. M. A. Dawson, and V. K. Goyal, "Dithered depth imaging," *Opt. Expr.*, vol. 28, pp. 35143–35157, Nov. 2020.

[55] M. P. Sheehan, J. Tachella, and M. E. Davies, "A sketching framework for reduced data transfer in photon counting lidar," *IEEE Trans. Comput. Imaging*, vol. 7, pp. 989–1004, 2021.

[56] V. Poisson, V. T. Nguyen, W. Guicquero, and G. Sicard, "Luminance-depth reconstruction from compressed time-of-flight histograms," *IEEE Trans. Comput. Imaging*, vol. 8, pp. 148–161, 2022.

[57] J. Tachella, M. P. Sheehan, and M. E. Davies, "Sketched RT3D: How to reconstruct billions of photons per second," in *Proc. IEEE Int. Conf. Acoust., Speech, and Signal Process.*, (Singapore), pp. 1566–1570, 2022.

[58] B. Schwarz, "LIDAR: Mapping the world in 3D," *Nature Photon.*, vol. 4, pp. 429–430, July 2010.

[59] J. Rapp, J. Tachella, Y. Altmann, S. McLaughlin, and V. K. Goyal, "Advances in single-photon lidar for autonomous vehicles: working principles, challenges, and recent advances," *IEEE Signal Process. Mag.*, vol. 37, pp. 62–71, July 2020.

[60] P. Cambou and T. Ayari, "With the Apple iPad LiDAR chip, Sony landed on the moon without us knowing." i-MicroNews https://www.i-micronews.com/with-the-apple-ipad-lidar-chip-sony-landed-on-the-moon-without-us-knowing/, 7 May 2020.

[61] C. Callenberg, Z. Shi, F. Heide, and M. B. Hullin, "Low-cost SPAD sensing for non-line-of-sight tracking, material classification and depth imaging," *ACM Trans. Graph.*, vol. 40, pp. 1–12, Aug. 2021. Art. no. 61.

[62] A. Ruget, M. Tyler, G. M. MartÃn, S. Scholes, F. Zhu, I. Gyongy, B. Hearn, S. McLaughlin, A. Halimi, and J. Leach, "Pixels2pose: Super-resolution time-of-flight imaging for 3d pose estimation," *Sci. Adv.*, vol. 8, no. 48, p. eade0123, 2022.

[63] R. A. Barton-Grimley, R. A. Stillwell, and J. P. Thayer, "High resolution photon time-tagging lidar for atmospheric point cloud generation," *Opt. Expr.*, vol. 26, p. 26030, Oct. 2018.

[64] M. Jaboyedoff, T. Oppikofer, A. Abellán, M.-H. Derron, A. Loye, R. Metzger, and A. Pedrazzini, "Use of LIDAR in landslide investigations: a review," *Nat. Hazards*, vol. 61, pp. 5–28, 2012.

[65] G. Luetzenburg, A. Kroon, and A. A. Bjørk, "Evaluation of the Apple iPhone 12 Pro LiDAR for an application in geosciences," *Sci. Rep.*, vol. 11, Nov. 2021.

[66] S. Tavani, A. Billi, A. Corradetti, M. Mercuri, A. Bosman, M. Cuffaro, T. Seers, and E. Carminati, "Smartphone assisted fieldwork: Towards the digital transition of geoscience fieldwork using LiDAR-equipped iPhones," *Earth-Sci. Rev.*, vol. 227, Apr. 2022.

[67] P. Rodríguez-Gonzálvez, B. J. Fernández-Palacios, Á. L. Muñoz-Nieto, P. Arias-Sanchez, and D. Gonzalez-Aguilera, "Mobile LiDAR system: New possibilities for the documentation and dissemination of large cultural heritage sites," *Remote Sens.*, vol. 9, no. 3, p. 189, 2017.

[68] J. W. Goodman, *Statistical Optics*. New York, NY, USA: Wiley, 1985.

[69] D. L. Snyder and M. I. Miller, *Random Point Processes in Time and Space*. Springer Science & Business Media, 2012.

[70] J. Tachella, Y. Altmann, S. McLaughlin, and J.-Y. Tourneret, "3D reconstruction using single-photon lidar data exploiting the widths of the returns," in *Proc. IEEE Int. Conf. Acoust., Speech, and Signal Process.*, pp. 7815–7819, May 2019.

[71] S. Cova, M. Ghioni, M. A. Itzler, J. C. Bienfang, and A. Restelli, "Semiconductor-based detectors," in *Single-Photon Generation and Detection* (A. Migdall, S. V. Polyakov, J. Fan, and J. C. Bienfang, eds.), ch. 4, pp. 83–146, Academic Press, 2013.

[72] M. J. Stevens, "Photon statistics, measurements, and measurements tools," in *Single-Photon Generation and Detection* (A. Migdall, S. V. Polyakov, J. Fan, and J. C. Bienfang, eds.), ch. 2, pp. 25–68, Academic Press, 2013.

[73] J. Zhang, M. A. Itzler, H. Zbinden, and J.-W. Pan, "Advances in InGaAs/InP single-photon detector systems for quantum communication," *Light Sci. Appl.*, vol. 4, p. e286, May 2015.

[74] I. M. Antolovic, C. Bruschini, and E. Charbon, "Dynamic range extension for photon counting arrays," *Opt. Expr.*, vol. 26, pp. 22234–22248, Aug. 2018.

[75] P. B. Coates, "The correction for photon 'pile-up' in the measurement of radiative lifetimes," *J. Phys. E: Sci. Instrum.*, vol. 1, pp. 878–879, Aug. 1968.

[76] S. C. Medin, J. Murray-Bruce, D. CastaÃ±Ã³n, and V. K. Goyal, "Beyond binomial and negative binomial: Adaptation in Bernoulli parameter estimation," *IEEE Trans. Comput. Imaging*, vol. 5, pp. 570–584, Dec. 2019.

[77] L. R. Varshney and V. K. Goyal, "Toward a source coding theory for sets," in *Proc. IEEE Data Compression Conf.*, (Snowbird, UT), pp. 13–22, Mar. 2006.

[78] M. O'Toole, F. Heide, D. B. Lindell, K. Zang, S. Diamond, and G. Wetzstein, "Reconstructing transient images from single-photon sensors," in *Proc. IEEE Conf. Comput. Vis. Pattern Recog.*, pp. 2289–2297, 2017.

[79] D. V. O'Connor and D. Phillips, *Time-correlated Single Photon Counting*. London: Academic Press, 1984.

[80] Y. Chen, J. D. Müller, P. T. So, and E. Gratton, "The photon counting histogram in fluorescence fluctuation spectroscopy," *Biophys. J.*, vol. 77, no. 1, pp. 553–567, 1999.

[81] I. Bar-David, "Communication under the Poisson regime," *IEEE Trans. Inform. Theory*, vol. 15, no. 1, pp. 31–37, 1969.

[82] "SPCM-AQRH single photon counting module." https://www.excelitas.com/file-download/download/public/60241?filename=

Excelitas_SPCM-AQRH_Family_datasheet.pdf. Excelitas (accessed Mar. 20, 2023).
[83] "MPD PDM series." http://www.micro-photon-devices.com/MPD/media/Datasheet/PDM.pdf. Micro Photon Devices (accessed Mar. 20, 2023).
[84] "Single photon detectors: SPDMH2, SPDMH3, SPDMH2F, SPDMH3F operation manual." https://www.thorlabs.com/drawings/c553f459d3842f5c-020B6CA5-9735-6CB3-539A0574D7195D37/SPDMH2-Manual.pdf. ThorLabs (accessed Mar. 20, 2023).
[85] "ID100 visible single photon detector." https://marketing.idquantique.com/acton/attachment/11868/f-0236/1/-/-/-/-/ID100_Brochure.pdf. ID Quantique (accessed Mar. 20, 2023).
[86] "quTAG Time-to-Digital Converter Manual V1.4." https://www.qutools.com/files/quTAG/quTAG-Manual_V1.4.0.pdf. (accessed Mar. 20, 2023).
[87] "Time Tagger Series." https://www.swabianinstruments.com/time-tagger/, 2023. Swabian Instruments (accessed Mar. 20, 2023).
[88] "TCSPC and Time Tagging Electronics." https://www.picoquant.com/products/category/tcspc-and-time-tagging-modules. PicoQuant (accessed Mar. 20, 2023).
[89] A. Ingle, A. Velten, and M. Gupta, "High flux passive imaging with single-photon sensors," in *Proc. IEEE Conf. Comput. Vis. Pattern Recog.*, pp. 6753–6762, June 2019.
[90] Y. Liu, F. Gutierrez-Barragan, A. Ingle, M. Gupta, and A. Velten, "Single-photon camera guided extreme dynamic range imaging," in *Proc. IEEE/CVF Winter Conf. Appl. Comput. Vis.*, pp. 41–51, 2022.
[91] P. E. Debevec and J. Malik, "Recovering high dynamic range radiance maps from photographs," in *ACM Trans. Graph.*, pp. 369–378, Aug. 1997.

Ruangrawee Kitichotkul (S'23) received the B.S. degree (with distinction) and M.S. degree in electrical engineering from Stanford University, Stanford, CA, USA in 2022. He is currently working toward the Ph.D. degree at the Department of Electrical and Computer Engineering, Boston University, Boston, MA, USA. His research interests include statistical signal processing and computational imaging. He is a member of IEEE and SIAM.

Joshua Rapp (S'12–M'20) received the B.S. degree in electrical engineering from Tufts University, Medford, MA, in 2014 and the M.S. and Ph.D. degrees in electrical engineering from Boston University, Boston, MA in 2016 and 2020, respectively.

He was a doctoral fellow at Draper, Cambridge, MA from 2015 to 2019 and a postdoctoral researcher with the Department of Electrical Engineering at Stanford University, CA from 2020 to 2021. He is currently a Research Scientist with Mitsubishi Electric Research Laboratories, Cambridge, MA. His research interests include computational imaging, optical sensing, lidar, and statistical signal processing.

Dr. Rapp is a member of IEEE, Optica, SIAM, Eta Kappa Nu, and Tau Beta Pi. He was the winner of the 2021 Best PhD Dissertation Award from the IEEE Signal Processing Society and the 2020 Best EE Dissertation Award from Boston University. His work also received a Best Student Paper Award at the IEEE International Conference on Image Processing in 2018 and a Young Author Best Paper Award from the IEEE Signal Processing Society in 2020.

Vivek K Goyal (S'92–M'98–SM'03–F'14) received the B.S. degree in mathematics and the B.S.E. degree in electrical engineering from the University of Iowa, where he received the John Briggs Memorial Award for the top undergraduate across all colleges. He received the M.S. and Ph.D. degrees in electrical engineering from the University of California, Berkeley, where he received the Eliahu Jury Award for outstanding achievement in systems, communications, control, or signal processing.

He was a Member of Technical Staff in the Mathematics of Communications Research Department of Bell Laboratories, Lucent Technologies, 1998–2001; and a Senior Research Engineer for Digital Fountain, Inc., 2001–2003. He was with the Massachusetts Institute of Technology 2004–2013, where he was the Esther and Harold E. Edgerton Associate Professor of Electrical Engineering. He was an adviser to 3dim Tech, Inc. (winner of the 2013 MIT $100K Entrepreneurship Competition Launch Contest Grand Prize), and was subsequently with Nest, an Alphabet company, 2014–2017. He is current a Professor of Electrical and Computer Engineering at Boston University, Boston, MA, USA.

Dr. Goyal is a member of Phi Beta Kappa and Tau Beta Pi. He was awarded the 2002 IEEE Signal Processing Society (SPS) Magazine Award, the 2014 IEEE Int. Conf. Image Processing Best Paper Award, and the IEEE SPS Best Paper Award in 2017 and 2019. He is also a recipient of a Frontiers of Science Award in the area of Computational Optics for a 2018 paper in *Science*. Work he supervised won student best paper awards at the IEEE Data Compression Conf. in 2006 and 2011, the 2012 IEEE Sensor Array and Multichannel Signal Processing Workshop, and the 2018 IEEE Int. Conf. Image Processing, as well as the 2020 IEEE SPS Young Author Best Paper Award and the 2021 IEEE SPS Best PhD Dissertation Award. He was a Co-chair of the SPIE Wavelets and Sparsity conference series 2006–2016. He current serves on the Editorial Boards of IEEE TRANS. COMPUTATIONAL IMAGING, SIAM J. IMAGING SCIENCES, and *Foundations and Trends in Signal Processing*. He is a Fellow of Optica and of the American Association for the Advancement of Science, and he is a co-author of *Foundations of Signal Processing* (Cambridge University Press, 2014).